



# Algorithm for *in vivo* detection of tissue type from multiple scattering light phase images

INBAR YARIV, HAMOOTAL DUADI, RUCHIRA CHAKRABORTY, AND DROR FIXLER\*

Faculty of Engineering and the Institute of Nanotechnology and Advanced Materials, Bar Ilan University, Ramat Gan 5290002, Israel

\*Dror.Fixler@biu.ac.il

**Abstract:** *In vivo* physiological assessments are typically done by either imaging techniques or by sensing changes in the attenuation coefficient. Using visible or near-infrared (NIR), imaging is mainly possible for thin tissues. On the other hand, clinical information can also be detected by examining changes in tissue optical properties. The most challenging aspect in sensing techniques is the spectral dependent scattering, which varies with the physiological state and tissue type. We have previously published our novel noninvasive nanophotonics technique for detecting tissue scattering based on reflectance measurements: the iterative multi-plane optical property extraction (IMOPE). The IMOPE reconstructs the reemitted light phase using an iterative algorithm and extracts the scattering properties based on a theoretical model. This paper presents the *in vivo* application of distinguishing between different mouse tissue areas. The reconstructed phase images reveal different areas in the inner thigh of a mouse, which are related to the muscle, bone, and skin. The IMOPE uses the reconstructed phases for sensing and detecting unseen components beneath the skin surface. This technique could be further applied to the diagnosis of various physiological states.

© 2019 Optical Society of America under the terms of the [OSA Open Access Publishing Agreement](#)

## 1. Introduction

For many years, the detection of objects hidden behind opaque materials was considered challenging due to their random multiple scattering ability. Opaque materials, e.g. walls, doors, tissues, and bones, were considered accounted for as barriers. In recent years looking behind walls seems to become more reality than just fiction with through-the-wall radar imaging (TWRI) [1,2] or X-ray vision [3,4] techniques used for activities detection behind walls. When focusing on the physiological barriers, i.e. tissues, these barriers are mainly imaged using X-ray for computed tomography (CT) scans [5,6], ultrasound [7,8] and radio waves for magnetic resonance imaging (MRI) [9,10]. All those techniques use electromagnetic wave irradiation with wavelengths outside the optical window. One very common imaging technique which utilizes the optical window is optical coherence tomography (OCT) [11,12]. As most of the optical imaging techniques, the OCT can acquire high-resolution images of the surface of thin tissues. When trying to optically detect components behind thick tissues it may be preferable to use sensing techniques rather than imaging. For detecting components behind or within tissues using the optical window, one will need to use some manipulations (wavefront shaping [13,14], speckle correlation [15–17], etc.) either on the irradiated or the reemitted light. Photons reemitted from opaque material have gone through multiple scattering and possess the material internal information. This information, which is useful in various fields such as biology, medicine, material science, security, and intelligence, can be extracted by detecting changes in the attenuation coefficient. The attenuation coefficient is composed of both the absorption and scattering properties which pose a challenge in terms of spatial resolution and single property detection.

We have suggested previously a noninvasive, nanophotonics technique for detecting tissue scattering, i.e. the iterative multi-plane optical property extraction (IMOPE) [18–22].

The IMOPE's fundamental idea is the relation between the light phase reemitted from the irradiated medium and its scattering properties. The reemitted light phase is reconstructed by the optical iterative Gerchberg-Saxton (GS) algorithm [23], which is known for beam shaping [24] and phase retrieval [25] for image reconstruction [26]. The GS algorithm uses captured intensity images and electromagnetic field propagation equations to reconstruct the phase that was lost once the images were captured. However, the IMOPE does not use the phase itself but rather its distribution, and specifically, the root mean square (RMS). Having the reemitted light phase RMS, the IMOPE compares it to a theoretical model. The radiative transport equation (RTE) [27] is the main approach to describe the propagation of light through tissues with the diffusion approximation being the most common analytical solution [28,29]. The steady state diffusion reflection (DR) theory is a widely known theory where the physical light source is represented by a sum of an isotropic source and an additional "image" source, based on the method of mirror images [30–32]. One known limitation of DR is that it's inadequate close to the source entrance point [33]. To answer that, Piao *et.al.* suggested a modification where a master-slave dual-source model is taken into account [34]. Having the dual-model theory, only the reflected intensity is described. Hence, we have proposed to define the phase as the product of the wavenumber and average pathlength [21,22], which depends on the differential pathlength factor (DPF) [32,35]. Using this theoretical model, we have shown a high fit of the theoretical phase RMS to tissue-like phantom experimentally obtained phase RMS [21,22]. In this paper, we present the application of the IMOPE technique with the aforementioned theoretical model for detecting the influence of different tissue types within a mouse inner thigh. The *in vivo* experimental results indicate the IMOPE ability to sense a mouse muscle, bone, and skin by computing the phase RMS from different areas of the reconstructed phase images.

## 2. Materials and methods

### 2.1. Iterative multi-plane optical properties extraction (IMOPE)

The IMOPE technique is composed of a theoretical model (described in [22]) and the iterative GS algorithm [23] combined with an experimental setup. The theoretical model links the reemitted light phase distribution to the reduced scattering coefficient ( $\mu_s'$ ) of a medium. The IMOPE technique starts with reconstructing the reemitted light phase using recorded light intensity images, and the GS algorithm, calculates the phase distribution, specifically the phase RMS, and compares the experimentally obtained results to the theoretical model for extracting the reduced scattering coefficient.

#### 2.1.1. Multiple measurement Gerchberg-Saxton algorithm

As mentioned previously, by using the multiple measurements GS algorithm the IMOPE algorithm reconstructs the reemitted light phase. Note, that the GS algorithm reconstructs the light phase that was lost based on electromagnetic field free space propagation (FSP) equations. The M planes used in the GS algorithm and the schematic sketch of the GS algorithm between two planes are presented in Fig. 1(a) and (b). The algorithm uses recorded intensity images,  $I_j$  at M planes; thereby the amplitude at each plane,  $A_j$ , can be computed by  $A_j = \sqrt{I_j}$ . Having  $A_j$  at each plane and an imposed initial random phase,  $\varphi_1$  at the first plane, we can calculate the estimated phase of the M<sup>th</sup> plane as follows (Fig. 1(b) describes steps 2.1.1- 2.1.4):

1. Set the input electrical field to be  $P_1 = A_1 e^{i\varphi_1}$
2. For planes  $j = 1, 2, \dots, M-1$ :
  - 2.1. For iterations  $t = 1, 2, \dots, T$ :

2.1.1. Propagate the light from  $P_j$  a distance of  $dz$  using the Fresnel FSP integral [36] to the next plane, resulting with a new electrical field  $\tilde{P}_{j+1} = \tilde{A}_{j+1} e^{i\varphi_{j+1}}$ .

2.1.2. Impose the magnitude of this field to be  $A_{j+1}$  (the measured amplitude at  $P_{j+1}$ ) and keep the received phase  $\varphi_{j+1}$  results in  $P_{j+1} = A_{j+1} e^{i\varphi_{j+1}}$ .

2.1.3. Propagate the field a distance of  $-dz$  back to  $P_j$  and replace the magnitude of the field to be the measured one,  $A_j$ , resulting in  $P_j = A_j e^{i\hat{\varphi}_j}$ .

2.1.4. Impose the random phase  $\varphi_j$  for the next iteration to be the received phase from the last iteration,  $\hat{\varphi}_j$ .

2.2. If  $j = M-1$ , calculate the intensity RMS,  $\varepsilon$ , using Eq. (1) If  $\varepsilon > \text{Threshold}$ , go back to step 2.1.1 for further iterations.

2.3. Set the new random phase for the next plane  $\varphi_{j+1}$  to be the obtained phase from step 2.1.2 after  $T$  iterations.

2.4. The next plane electrical field is now  $P_{j+1} = A_{j+1} e^{i\varphi_{j+1}}$ .

2.5. Continue to step 2 with the next two planes.

At the end of the above algorithm, i.e., when  $j = M-1$  and  $\varepsilon < \text{Threshold}$ , the estimated light phase of the last plane  $\varphi_M$  is received.

The Intensity RMS,  $\varepsilon$ , mentioned at step 2.1.5 is calculated as follows:

$$\varepsilon = \sqrt{\frac{1}{N^2} \sum_{x,y \in \gamma} |\tilde{A}_M(x,y) - A_M(x,y)|^2} \quad (1)$$

where  $N^2$  is the total number of pixels in our matrix,  $A_M(x,y)$  is the measured amplitude at  $P_M$ ,  $\tilde{A}_M(x,y)$  is the amplitude obtained after the Fresnel FSP integral (received at step 2.1.1) and  $\gamma$  is the spatial region of interest.

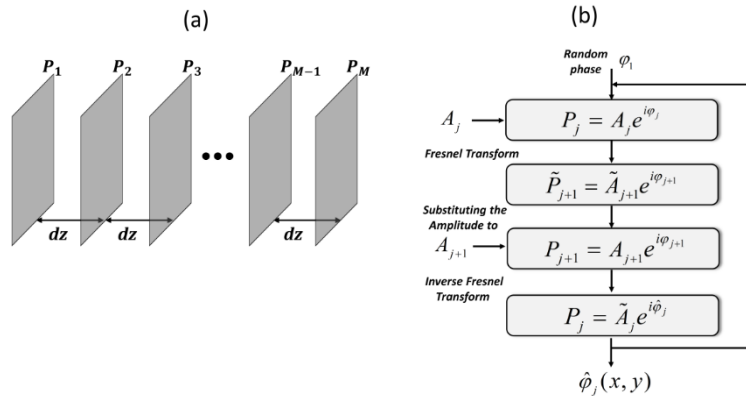


Fig. 1. (a) Light intensity images of  $M$  planes for the multiplane GS algorithm. (b) A schematic sketch of the GS algorithm with two planes. The algorithm operates between every two planes iteratively until it stops according to the threshold (Eq. (1)) and continues to the next two planes with the computed phase  $\varphi_{j+1}$ .

### 2.1.2. Experimental setup

The phase is reconstructed by the multiple measurement GS algorithm using recorded light intensity images. Hence, a noninvasive reflection based experimental setup was designed (Fig. 2) to record multiple reflected light intensity images, separated by a distance  $dz$ . The setup is composed of a Helium-Neon (He-Ne) gas laser with a wavelength of  $\lambda = 632.8\text{nm}$  and power of  $3.4\text{mW}$ , polarizers (LPVISE100-A, Thorlabs, Japan) for optical clearing purposes (where the first polarizer positioned where the maximum intensity is received, and the second polarizer is positioned in 90 degrees to it in order to clear the surface reflection) [37], a lens (focal length of  $f = 75\text{mm}$ ) in order to focus the light beam and a CMOS camera (DCC1545M, Thorlabs, Japan). The lens, polarizer, and camera were set on a micrometer stage (distanced to receive a magnitude of 1) with an angle of  $14.5^\circ$  from the laser source; hence, the images were corrected accordingly. The samples were held by an adjustable holder, which was set on a 3-axis micrometer stage for fine-tuning during experiments. For each sample, the intensity images were recorded at multiple planes, by moving the entire camera-polarizer-lens assembly.

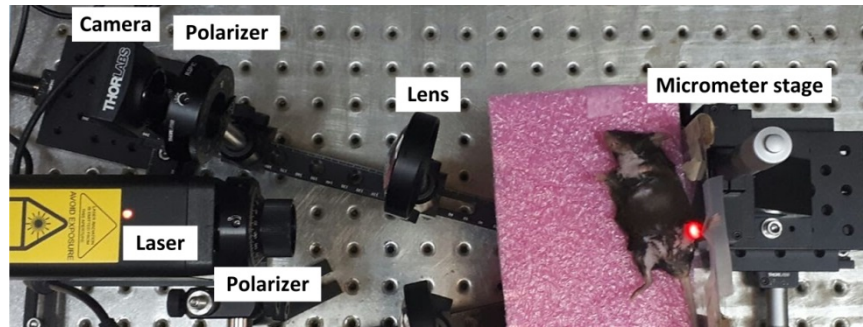


Fig. 2. The experimental setup for recording light intensity images. An image of the setup and its components. The camera records images at multiple planes with equal intervals between them. The experimental setup was designed for reflection measurements. The light source is a He-Ne gas laser with  $\lambda = 632.8\text{nm}$ , the focal length of the lens is  $75\text{mm}$ ; polarizers were added for optical clearing purposes. The sample is set on three axis micrometer plates and can be adjusted in the x-y-z directions.

### 2.1.3. IMOPE algorithm

The IMOPE algorithm for extracting  $\mu_s'$  (Fig. 3(a)), starts with the reconstruction of the remitted light phase  $\hat{\phi}_M(x, y)$ , by applying the multiple measurement GS algorithm with  $M$  light intensity images and the threshold conditions as detailed in the former section. The average value of the reconstructed phase is calculated and subtracted from the received phase image. The image of the reconstructed phase is then used for calculating the phase distribution, specifically, its RMS based on:

$$RMS_{\phi_M} = \frac{\sqrt{\sum_{x,y \in \gamma} |A_M(x, y)e^{i\hat{\phi}_M(x, y)} - A_M(x, y)e^{i\phi_M(x, y)}|^2}}{\sqrt{\sum_{x,y \in \gamma} |A_M(x, y)|^2}} \quad (2)$$

where  $A_M(x, y)$  is the amplitude at the desired  $M^{\text{th}}$  plane along  $z$ ,  $\gamma$  is the spatial region of interest,  $\hat{\phi}_M(x, y)$  is the reconstructed phase accumulated at the desired plane following propagating a distance of  $D$  and  $\phi_M(x, y)$  is set to be zero. Note, that the final reconstructed phase values,  $\hat{\phi}_M(x, y)$ , vary in the range of  $[-\pi, \pi]$ . Hence, since we are looking for the

distance between the phase and  $0^\circ$ , negative and positive phase values will have the same influence on the RMS calculations. Following computing the phase RMS, the reduced scattering coefficient can be extracted by comparing the results to the theoretical model.

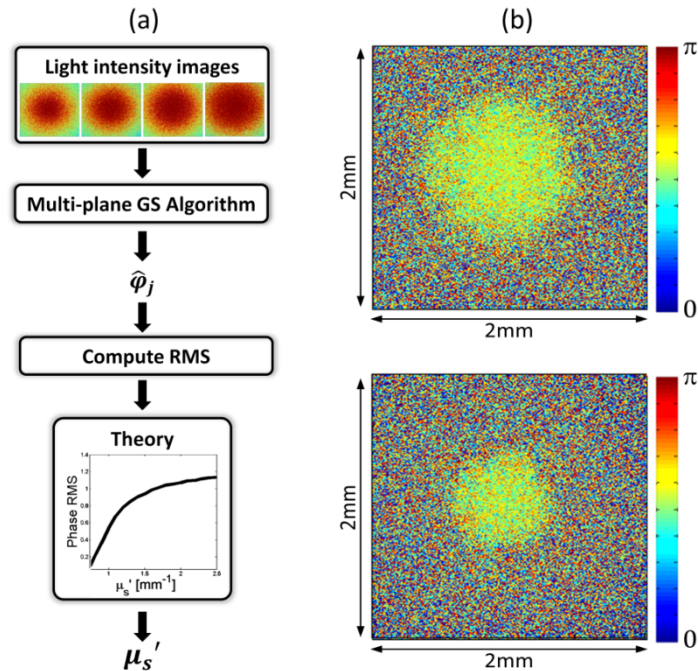


Fig. 3. (a) A schematic description of the IMOPE algorithm for reconstructing  $\mu_s'$ . After running the multi-plane GS algorithm with the threshold conditions between every two planes, the estimated phase  $\hat{\phi}_j$  is retrieved. The RMS is calculated and produces an estimation for  $\mu_s'$  compared to the theory (as described in Eq. (2)). (b) Reconstructed absolute light phase images from tissue-like phantom with  $\mu_s' = 0.9 \text{ mm}^{-1}$  and  $1.3 \text{ mm}^{-1}$  (top and bottom respectively).

We have published previously [21,22] how the reconstructed light phase images of homogeneous solid tissue like phantoms (Fig. 3(b), top and bottom corresponds to  $\mu_s' = 0.9 \text{ mm}^{-1}$  and  $1.3 \text{ mm}^{-1}$  respectively) show two distinguishable areas. A circle area which was found to correspond to the single scattering regime and the area outside of the circle (which was labeled as a ring) to the multiple scattering regime. As the phantoms were homogeneous the border between those two regimes was a circle with a radius of approximately  $1/\mu_s'$ .

## 2.2. In vivo experiments

A C57BL male mouse (age 4.5 months) was anesthetized using 200  $\mu\text{L}$  of a mixture of ketamine 100mg/mL + xylazine 20mg/mL injected intraperitoneally. The mouse was laid on a flat surface with its inner thigh facing the laser (its hair was removed pre-measurements); it was placed on a sample holder, set on a 3-axis micrometer stage for fine tuning during experiments, and fixed to the polycarbonate mount. The surface of the mouse skin was kept perpendicular to the direction of the incident laser beam through the experiments.

This study received institutional approval from the Bar Ilan University Institutional Animal Care and Use Committee. All *in vivo* measurements were performed under appropriate anesthesia: the mice barrier-controlled facility followed the Bar Ilan's University Animal Care and Use Committee guidelines. The veterinarian, who handles the appropriate tests and treatment protocols, as required, inspected the mouse daily. All research protocols were followed closely by the veterinarian. All major procedures were performed in the surgical facilities using general anesthesia and standard, aseptic surgical techniques [38,39].



### 3. Results: characterization of different tissue areas

In order to extract the reduced scattering coefficient of different tissues, the IMOPE compares the experimentally obtained RMSs to a theoretical model, as described in section 2.1.3. The theoretical reflected light phase and its RMS are described in full details in [22]. In this model, the reflectance intensity from a semi-infinite homogeneous medium is described by using the master-slave dual-source configuration suggested by Piao *et al* [34]. For the reflected phase, however, as the DR theory lacks in phase description, we have suggested describing the phase as the product of the wavenumber and the average pathlength which depends on the differential path length factor (DPF) [21,22].

$$\phi(x, y) = \frac{2\pi n}{\lambda} DPF \cdot \sqrt{x^2 + y^2} \quad (3)$$

where  $n$  is the refractive index and  $\lambda$  is the wavelength.

The relation between the phase RMS and  $\mu_s'$ , for the multiple scattering regime (presented in Fig. 4), was founded based on our theoretical model. For this regime, the RMS increases with increasing the scattering properties. Given the theoretical dependence of the RMS on  $\mu_s'$ , the scattering properties of tissues can be extracted.

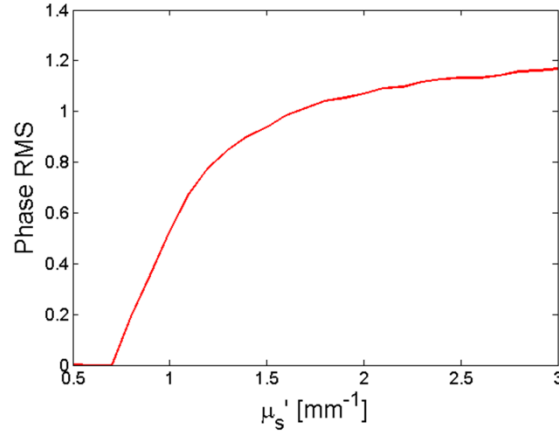


Fig. 4. Theoretically computed phase RMS for the multiple scattering regime.

*In vivo* experiments were performed on a mouse as detailed in section 2.2 and three different positions on the inner thigh surface were measured, as can be seen in Fig. 5(a). The phase was reconstructed by applying the multi-plane GS algorithm (section 2.1.1) with  $M = 7$  light intensity images at the size of 2mm X 2mm,  $dz = 0.635\text{mm}$  the distance between images and the threshold condition. All those parameters were chosen according to the tissue-like phantom calibration experiments which were performed previously [22] with high compatibility to our theoretical model presented here in Fig. 4. Note that, the product of the number of planes ( $M$ ) and the distance between them ( $dz$ ) has to be higher than the transport mean free path (MFP') in order to be in the multiple scattering regime. Looking at the reconstructed phase images, acquired at different spatial positions ( $x, y$ ) and at the same depth ( $z$ ), (Figs. 5(b)-(d)) there are a few distinguishable areas. The single scattering regime was marked with a black dashed circle and the different areas in the multiple scattering regime were marked with red and white circles (1-5 in Figs. 5(b)-(d)) in each image. In contrary to the reconstructed phase images obtained from tissue-like phantoms (2.1.3 Fig. 3), where the border between the different areas was a clear circle, the phase images reconstructed from the *in vivo* measurements have a few areas in one image and the border between them is not so discernible. The reason for that is the heterogeneity of the inner thigh of the mouse as

opposed to homogeneous phantom. Each point measured from the mouse's inner thigh is influenced by deeper components in its environment. For each of the 5 areas numbered in Figs. 5(b)-(d), the RMS of the phase was calculated and their values are presented in Table 1. The reduced scattering coefficient, which was extracted using the theoretical model presented in Fig. 4, is also shown in Table 1. Areas 1 and 2 have produced  $\mu_s' > 2.5\text{mm}^{-1}$  which was found in the literature [40] to be related to a mouse bone. Note that, in the current optical configuration (with a magnification of 1),  $2.5\text{mm}^{-1}$  is the upper limit of the measurements range. In area 3 the extracted  $\mu_s'$  was between  $0.5\text{mm}^{-1}$  and  $0.9\text{mm}^{-1}$ , where  $\mu_s' = 0.5\text{mm}^{-1}$  was reported for mouse muscle [40]. Area 5, which its phase image looks very similar to the first two areas (1 and 2), produced  $\mu_s' \sim 2.5\text{mm}^{-1}$ . This value was reported before with relation to mouse skin [40]. Finally, area 4 produced  $\mu_s' \sim 0.9\text{mm}^{-1}$ , as this value was not reported in the literature, we suspect is to be a complex of different tissue types combined together. For complex structures where few tissue types are mixed together, a comparison with additional sensing or imaging modalities will add the missing information for a better and more accurate IMOPE detection. Nevertheless, the reconstructed phase images reveal unseen components behind the skin surface. Note that the IMOPE is able to sense the influence of single tissue type with high precision. However, the accuracy on the exact (x,y) location of each tissue type is not yet feasible based on the reconstructed phase images and the RMS values.

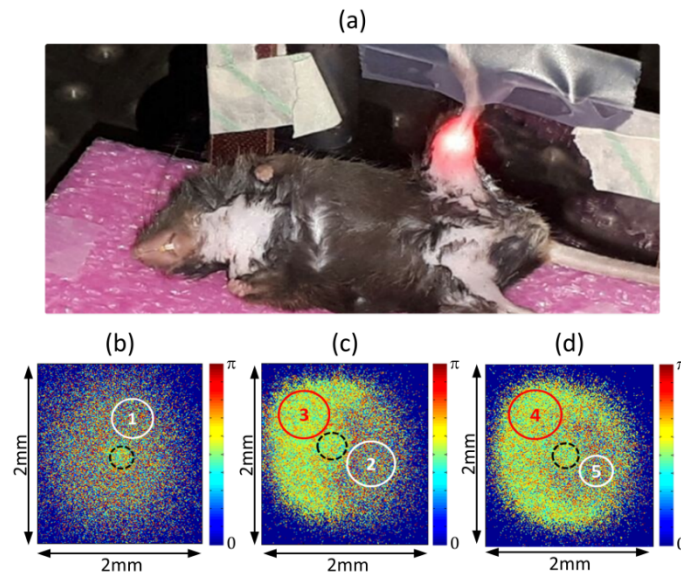


Fig. 5. Phase images of different areas in a mouse inner thigh. (a) The mouse placed on the IMOPE sample stage with the laser radiating its inner thigh. (b)-(d) the reconstructed absolute phase images of three different positions at the inner thigh of the mouse. The phase reconstructed using the multi-plane GS algorithm as mention in section 2.1.1 with  $M = 7$  intensity planes,  $dz = 0.635\text{mm}$ , and images of  $2\text{mm} \times 2\text{mm}$ .

Table 1. Differentiation between different tissue types according to the RMS values based on the reconstructed phase images.

Area	1	2	3	4	5
RMS	1.40	1.32	0.42	0.54	1.25
$\mu_s' [\text{mm}^{-1}]$	$>2.5$	$>2.5$	$0.5-0.9$	$\sim 0.9$	$\sim 2.5$

#### 4. Conclusions

This paper presents the *in vivo* application of the nanophotonics IMOPE technique for detecting different tissue types of a mouse. The IMOPE extracts the scattering properties of a

medium by a combination of an experimental setup and an iterative algorithm for phase reconstruction. We have previously suggested the use of the phase RMS as an indicator for turbid medium reduced scattering coefficient based on tissue-like phantom experiments. First, the reflected light phase is reconstructed using the GS algorithm and light intensity images recorded in the experimental setup. Then by looking at the reconstructed phase images, distinguishable areas are marked, the RMS is computed from each area and compared to the theoretical phase RMS under the same reconstruction conditions. In this paper, we present how by computing the phase RMS, at different areas in the reconstructed phase images, various tissue types can be detected. The IMOPE, as a sensing technique, detected the influence of hidden components under the skin surface such as muscle and bone with high precision.

## Disclosures

The authors declare that there are no conflicts of interest related to this article.

## References

1. M. G. Amin, *Through-the-Wall Radar Imaging* (CRC press, 2017).
2. S. Sinha and H. C. Ferreira, "Through-the-Wall Radar Imaging: A Review AU - Nkwari, P. K. M.," *IETE Tech. Rev.* **35**(6), 631–639 (2018).
3. S. Depatla, L. Buckland, and Y. Mostofi, "X-Ray Vision With Only WiFi Power Measurements Using Rytov Wave Models," *IEEE Trans. Vehicular Technol.* **64**(4), 1376–1387 (2015).
4. D. Mery, E. Svec, M. Arias, V. Rizzo, J. M. Saavedra, and S. Banerjee, "Modern Computer Vision Techniques for X-Ray Testing in Baggage Inspection," *IEEE Trans. Syst. Man Cybern. Syst.* **47**(4), 682–692 (2017).
5. K.-D. Kim, A. Ruprecht, G. Wang, J. B. Lee, D. V. Dawson, and M. W. Vannier, "Accuracy of facial soft tissue thickness measurements in personal computer-based multiplanar reconstructed computed tomographic images," *Forensic Sci. Int.* **155**(1), 28–34 (2005).
6. E. Pauwels, D. Van Loo, P. Cornillie, L. Brabant, and L. Van Hoorebeke, "An exploratory study of contrast agents for soft tissue visualization by means of high resolution X-ray computed tomography imaging," *J. Microsc.* **250**(1), 21–31 (2013).
7. O. T. von Ramm and S. W. Smith, "Real time volumetric ultrasound imaging system," *J. Digit. Imaging* **3**(4), 261–266 (1990).
8. K. K. Shung, *Diagnostic Ultrasound: Imaging and Blood Flow Measurements* (CRC press, 2015).
9. J. Stefanowska, D. Zakowiecki, and K. Cal, "Magnetic resonance imaging of the skin," *J. Eur. Acad. Dermatol. Venereol.* **24**(8), 875–880 (2010).
10. R. Di Corato, F. Gazeau, C. Le Visage, D. Fayol, P. Levitz, F. Lux, D. Letourneur, N. Luciani, O. Tillement, and C. Wilhelm, "High-Resolution Cellular MRI: Gadolinium and Iron Oxide Nanoparticles for in-Depth Dual-Cell Imaging of Engineered Tissue Constructs," *ACS Nano* **7**(9), 7500–7512 (2013).
11. A. G. Podoleanu, "Optical coherence tomography," *Br. J. Radiol.* **78**(935), 976–988 (2005).
12. M. A. Fox, D. G. Diven, K. Sra, A. Boretzky, T. Poonawalla, A. Readinger, M. Motamedi, and R. J. McNichols, "Dermal scatter reduction in human skin: A method using controlled application of glycerol," *Lasers Surg. Med.* **41**(4), 251–255 (2009).
13. I. M. Vellekoop, A. Lagendijk, and A. P. Mosk, "Exploiting disorder for perfect focusing," *Nat. Photonics* **4**(5), 320–322 (2010).
14. Y. Liu, C. Ma, Y. Shen, J. Shi, and L. V. Wang, "Focusing light inside dynamic scattering media with millisecond digital optical phase conjugation," *Optica* **4**(2), 280–288 (2017).
15. D. Fixler, J. Garcia, Z. Zalevsky, A. Weiss, and M. Deutsch, "Speckle random coding for 2D super resolving fluorescent microscopic imaging," *Micron* **38**(2), 121–128 (2007).
16. J. A. Newman, Q. Luo, and K. J. Webb, "Imaging Hidden Objects with Spatial Speckle Intensity Correlations over Object Position," *Phys. Rev. Lett.* **116**(7), 073902 (2016).
17. Y. Li, Y. Xue, and L. Tian, "Deep speckle correlation: a deep learning approach toward scalable imaging through scattering media," *Optica* **5**(10), 1181–1190 (2018).
18. I. Yariv, G. Rahamim, E. Shliselberg, H. Duadi, A. Lipovsky, R. Lubart, and D. Fixler, "Detecting nanoparticles in tissue using an optical iterative technique," *Biomed. Opt. Express* **5**(11), 3871–3881 (2014).
19. I. Yariv, Y. Kapp-Barnea, E. Genzel, H. Duadi, and D. Fixler, "Detecting concentrations of milk components by an iterative optical technique," *J. Biophotonics* **8**(11-12), 979–984 (2015).
20. I. Yariv, M. Haddad, H. Duadi, M. Motiei, and D. Fixler, "New optical sensing technique of tissue viability and blood flow based on nanophotonic iterative multi-plane reflectance measurements," *Int. J. Nanomedicine* **11**, 5237–5244 (2016).
21. I. Yariv, H. Duadi, and D. Fixler, "Optical method to extract the reduced scattering coefficient from tissue: theory and experiments," *Opt. Lett.* **43**(21), 5299–5302 (2018).



22. I. Yariv, H. Duadi, and D. Fixler, *An Optical Method to Detect Tissue Scattering: Theory, Experiments and Biomedical Applications*, SPIE BiOS (SPIE, 2019), Vol. 10891.
23. R. W. Gerchberg and W. O. Saxton, "A practical algorithm for the determination of phase image and diffraction plane pictures," *Optik (Stuttg.)* **35**, 237–246 (1972).
24. Z. Zalevsky, D. Mendlovic, and R. G. Dorsch, "Gerchberg-Saxton algorithm applied in the fractional Fourier or the Fresnel domain," *Opt. Lett.* **21**(12), 842–844 (1996).
25. D. Ferber, "Livestock Feed Ban Preserves Drugs' Power," *Science* **295**(5552), 27–28 (2002).
26. D. Fixler, H. Duadi, R. Ankri, and Z. Zalevsky, "Determination of coherence length in biological tissues," *Lasers Surg. Med.* **43**(4), 339–343 (2011).
27. W.-F. Cheong, S. A. Prahl, and A. J. Welch, "A review of the optical properties of biological tissues," *IEEE J. Quantum Electron.* **26**(12), 2166–2185 (1990).
28. R. C. Haskell, L. O. Svaasand, T.-T. Tsay, T.-C. Feng, M. S. McAdams, and B. J. Tromberg, "Boundary conditions for the diffusion equation in radiative transfer," *J. Opt. Soc. Am. A* **11**(10), 2727–2741 (1994).
29. T. Tarvainen, M. Vauhkonen, V. Kolehmainen, S. R. Arridge, and J. P. Kaipio, "Coupled radiative transfer equation and diffusion approximation model for photon migration in turbid medium with low-scattering and non-scattering regions," *Phys. Med. Biol.* **50**(20), 4913–4930 (2005).
30. T. J. Farrell, M. S. Patterson, and B. Wilson, "A diffusion theory model of spatially resolved, steady-state diffuse reflectance for the noninvasive determination of tissue optical properties in vivo," *Med. Phys.* **19**(4), 879–888 (1992).
31. P. R. Bargo, S. A. Prahl, T. T. Goodell, R. A. Slevin, G. Koval, G. Blair, and S. L. Jacques, "In vivo determination of optical properties of normal and tumor tissue with white light reflectance and an empirical light transport model during endoscopy," *J. Biomed. Opt.* **10**(3), 034018 (2005).
32. D. Piao, R. L. Barbour, H. L. Graber, and D. C. Lee, "On the geometry dependence of differential pathlength factor for near-infrared spectroscopy. I. Steady-state with homogeneous medium," *J. Biomed. Opt.* **20**(10), 105005 (2015).
33. R. Ankri, H. Taitelbaum, and D. Fixler, "On Phantom experiments of the photon migration model in tissues," *The Open Optics Journal* **5**(1), 28–32 (2011).
34. D. Piao and S. Patel, "Simple empirical master-slave dual-source configuration within the diffusion approximation enhances modeling of spatially resolved diffuse reflectance at short-path and with low scattering from a semi-infinite homogeneous medium," *Appl. Opt.* **56**(5), 1447–1452 (2017).
35. D. T. Delpy, M. Cope, P. van der Zee, S. Arridge, S. Wray, and J. Wyatt, "Estimation of optical pathlength through tissue from direct time of flight measurement," *Phys. Med. Biol.* **33**(12), 1433–1442 (1988).
36. D. Mendlovic, Z. Zalevsky, and N. Konforti, "Computation considerations and fast algorithms for calculating the diffraction integral," *J. Mod. Opt.* **44**(2), 407–414 (1997).
37. V. V. Tuchin, L. Wang, and D. A. Zimnyakov, *Optical Polarization in Biomedical Applications* (Springer Science & Business Media, 2006).
38. N. Alon, T. Havdala, H. Skaat, K. Baranes, M. Marcus, I. Levy, S. Margel, A. Sharoni, and O. Shefi, "Magnetic micro-device for manipulating PC12 cell migration and organization," *Lab Chip* **15**(9), 2030–2036 (2015).
39. M. Motiei, T. Dreifuss, O. Betzer, H. Panet, A. Popovtzer, J. Santana, G. Abourbeh, E. Mishani, and R. Popovtzer, "Differentiating Between Cancer and Inflammation: A Metabolic-Based Method for Functional Computed Tomography Imaging," *ACS Nano* **10**(3), 3469–3477 (2016).
40. G. Alexandrakis, F. R. Rannou, and A. F. Chatziioannou, "Tomographic bioluminescence imaging by use of a combined optical-PET (OPET) system: a computer simulation feasibility study," *Phys. Med. Biol.* **50**(17), 4225–4241 (2005).